Journal of Alloys and Compounds 854 (2021) 156723

Contents lists available at ScienceDirect

Journal of Alloys and Compounds

journal homepage: http://www.elsevier.com/locate/jalcom

Nanoscale serration characteristics of additively manufactured superalloys

Russell A. Rowe [a, 1], Ali Tajyar [a, 1], Michael Munther [a], Kurt E. Johanns [b], Paul G. Allison [a], Kasra Momeni [a, **], Keivan Davami [a, *]

[a] Department of Mechanical Engineering, The University of Alabama, Tuscaloosa, AL, USA
[b] KLA Instruments, Oak Ridge, TN, USA

ARTICLE INFO

Article history:
Received 23 May 2020
Received in revised form
13 July 2020
Accepted 13 August 2020
Available online 15 August 2020

Keywords:
Nanoindentation
Nickel-based Superalloy
Inconel 625
Direct metal laser sintering
Serrated plastic flow

ABSTRACT

Structural elements made of nickel-based superalloys usually operate at high temperatures. Many surface failure mechanisms such as creep, fatigue, fretting fatigue, corrosion, and stress corrosion cracking start from the surface. Thus, studying the surface mechanical properties and deformation behavior of materials is vital in order to draw a correlation between the surface properties and failures. Herein, a nanoindentation technique was implemented to characterize surface properties of a widely used additively manufactured (AM) superalloy, i.e., Inconel 625. The specimens were tested in a range of temperatures in a vacuum chamber. Serrated plastic flow characterized by pop-in events during nanoindentation, known as Portevin-Le Chatelier (PLC) effect, was observed in all three tested elevated temperatures. This phenomenon depicts itself as bursts of plasticity in the loading section of the load-displacement curves. These bursts were studied comprehensively to explore incipient plasticity. Hertzian contact mechanics were implemented to extract the maximum shear stress beneath the indenter from the pop-in loads. The results show that the initial pop-in load increases as the temperature increases. The average initial pop-in load increases by almost four times from 300 °C to 650 °C. This was attributed to the formation of strengthening precipitates. The average size of the serrations and the magnitude of dislocation nucleation increase from 300 °C to 500 °C and decrease from 500 °C to 650 °C. The serrations are attributed to the dislocation generation and movement as well as their interaction with the solute atoms and precipitates.

1. Introduction

Metal 3D printing is a versatile additive manufacturing process that produces parts from the source material, either in the powder or solid forms, layer-by-layer directly from a digital model. This technique enables the fabrication of a wide range of advanced structures and devices that enhance the efficiency of the supply chain for both military and civilian applications. Currently, metal 3D printers are capable of printing a wide variety of materials including stainless steel [1], metal alloys [2–4], high entropy alloys [5], superalloys [6–8], and functionally graded materials [9]. Additive manufacturing is more material-efficient and customizable than traditional manufacturing due to the layer-by-layer building pattern. With layer-by-layer building, additive manufacturing is capable of fabricating more complex [10], and lighter components [11,12] than traditional manufacturing.

Superalloys are among the top material choices and other means of achieving high operating temperatures where the highest reliability and cost-effectiveness are needed [13]. Their ability to withstand extreme thermal and mechanical stress conditions make them applicable for a variety of applications, for instance in aircraft and industrial gas turbines. Inconel 625 is a widely used superalloy that can be additively manufactured via different techniques, of particular interest is direct metal laser sintering (DMLS). Various constituent phases are formed in DMLS printing of Inconel 625, and their quantity and distribution are a function of local temperatures, scanning speed, local cooling rates, and local compositions in the melt pool [14–16]. The primary strengthening mechanism for Inconel 625 is the precipitation of the Ni_3Nb gamma double prime (γ'') phase [17,18]. At 650 °C Inconel 625 experiences a large strengthening effect due to γ'' precipitation [19,20], however at temperatures greater than 650 °C the γ'' phase becomes unstable and starts to coarsen and then

---

* Corresponding author.
** Corresponding author.
E-mail addresses: kmomeni@ua.edu (K. Momeni), kdavami@eng.ua.edu (K. Davami).
[1] These authors contributed equally.

https://doi.org/10.1016/j.jallcom.2020.156723
0925-8388/

transform into δ phase, which at large quantities can be detrimental to the mechanical properties of Inconel 625 [19].

Nanoindentation is a versatile technique capable of characterizing various mechanical properties such as hardness and modulus [21–23], creep [24,25], and wear [25–27] at the nanoscale at room and elevated temperatures. In-situ [28,29] as well as ex-situ [30,31] nanoindentation shed lights on the scale-dependent plasticity properties and their connection with dislocation behavior, strengthening phases [32–34], and activated slip systems [35]. This technique has also been used to locally characterize the mechanical properties of AM superalloys [23,36,37]. Wang et al. [31] compared the nanomechanical properties of AM and traditionally manufactured (TM) Inconel 718 at room temperature, 350 °C, and 650 °C. It was shown that reduced modulus decreased by 26% for the TM specimens and by 22% for AM samples as the temperature rose from room temperature to 650 °C. The nanoindentation hardness reduced by 19% for the TM specimens and 16% for the AM samples. In- situ nanoindentation testing on additively manufactured Al with nanotwins indicates that in the early stages of deformation, the strain hardening effect is dominated by dislocation nucleation [29]. Exposure to hydrogen, which has been proven to restrict dislocation nucleation, has been shown to increase the hardness value for Inconel 718, indicating that an increased hardness is related to restricting dislocation nucleation [38].

A type of plastic instability, the Portevin–Le Chatelier effect (PLC), attributed to the diffusing solutes pinning dislocations and dislocations breaking away, presents itself with repetitive yielding in the stress-strain curves. This leads to the occurrence of a serrated stress–strain curve or jerky flow when the material undergoes plastic deformation in a certain range of temperatures and strain rates [39]. The dynamic interaction between mobile dislocations and diffusing solute atoms is called dynamic strain aging (DSA). The strain rate sensitivity of the flow stress is a key parameter in the PLC effect where the negative strain rate sensitivity makes the plastic flow unstable and the PLC effect occurs [40]. A relatively high temperature and low strain rate are required for the solute atoms to re-position themselves or diffuse to the dislocations and pin the dislocations. After pinning, additional stresses are needed to continue deformation by mobilizing the dislocation and the process repeats [41]. Other parameters such as precipitates [41,42], grain size [43,44], and material finish influence the PLC effect. Inhomogeneous deformation intensifies the PLC effect in many solid solutions [45,46].

DSA is the main reason behind the PLC effect [47]. DSA occurs in various Ni-base superalloys containing interstitial alloying additions such as boron and carbon, leading to the serrated plastic flow [48–50]. Serrated plastic flow can be observed in both constant loading rate as well as constant load experiments [51]. In the former, the material response is mostly affected by the dislocation nucleation and, in the latter, by dislocation movement [28]. Serrated plastic flow has been reported both at the nanoscale [52,53] and the macroscale [54]. Since the PLC effect is associated with highly localized deformation, it can significantly affect the performance of the material [55,56]. At the macroscale, it has been shown to negatively affect material properties such as fracture resistance. It can also degrade low-cycle fatigue life and reduce ductility [44,57–59]. Valsan et al. [58] reported that the PLC effect in Niomonic PE 16 superalloy makes the material more prone to internal grain-boundary cracks and reduced fatigue life due to the strain localization. At the microscale regime, it has been reported that the dislocation microstructures are dramatically different in the PLC and non-PLC regimes that also leads to different material responses and damage modes [41]. In addition, the PLC effect can be combined with other effects such as embrittlement by environmental conditions or stress corrosion cracking and result in catastrophic material failure [55]. Therefore, studying this effect in materials with critical applications, such as Ni-based superalloys, for their effective use is vital [60–62].

It was previously reported that in addition to the type of the material, various parameters including surface preparation [63], temperatures [64], indenter shape and its radius [65,66], solid solutions and their quantity [67], duration of the loading [68], and strain rate [5,69] affect the serrations in the nanoindentation process. In this report, nanomechanical testing of additively manufactured Inconel 625 was conducted, and the effect of the temperature was investigated. Three different temperatures, namely 300 °C, 500 °C, and 650 °C, were tested. The serrated plastic flow was observed and characterized in all different tested temperatures. The force-displacement data was precisely analyzed. Hertzian contact mechanics were implemented to extract the maximum shear stress beneath the indenter from the pop-in loads.

2. Experimental technique

Specimen fabrication was conducted using a Renishaw AM250 DMLS system (Renishaw Inc., IL, USA). The DMLS process utilizes a 200 W ytterbium fiber laser inside a chamber containing a precisely controlled atmosphere of argon gas. The source material was prealloyed atomized fine metal powder with particle sizes in the range of 24–53 μm (see powder composition in Table S1, Section 1, Supplementary Information). Thin layers of the metal powder with a layer height of 30 μm were evenly distributed using an automatic coating mechanism, consecutively. After each layer was formed, the laser beam was guided in the X and Y directions to fully fused the powder and create a 2D slice of the part geometry. This process was repeated until the part was fabricated layer by layer through selectively melting the powder. Bulk cylindrical specimens with a diameter of 10 mm were built parallel to the XY plane and sectioned into separate, 4 mm-thick disks via wire electric discharge machining (W-EDM). Sectioned samples were mechanically ground using sandpaper of successively finer grits (400, 600, 800, and 1200) followed by vibratory polishing in a 0.02 μm colloidal silica solution to prepare the material surface for nanoindentation. Investigation of the material surface following polishing resulted in surface roughness of ~50 nm.

A scanning electron microscope (Thermo Scientific™ Apreo) equipped with energy dispersive spectroscopy (EDS) and electron backscatter diffraction (EBSD) was implemented for the specimen characterization. The EBSD was performed employing a 10 kV acceleration voltage. The EBSD maps were obtained at an optimal working distance of 16 mm using a step size of 0.3 μm. Nanoindentation testing was performed in a vacuum chamber using an InSEM HT Nanoindenter (KLA Instruments, TN, USA). Both the indenter tip and sample were equipped with independent resistive heating elements for temperature control (Fig. S1, Section 2, Supplementary Information). Sufficient stabilization time was applied to minimize thermal artifacts during testing. Before each measurement, the tip and sample were at the same temperature with very small fluctuations (Fig. S2, Section 3, Supplementary Information). A Tungsten Carbide (WC) Berkovich indenter tip with a contact area function having been calibrated at room temperature on fused silica was used for all testing temperatures (Fig. S3, Section 4, Supplementary Information). At each temperature, 30 indents were performed and a maximum load of 50 mN was applied using a constant indentation strain rate of 0.4 s^{-1}. Elastic modulus and hardness were quantified as a function of indenter displacement by standard nanoindentation techniques [70] using the continuous stiffness measurement technique (Figs. S4 and S5).

3. Results and discussion

Fig. 1(a) shows the load-displacement (P-h) curves for 300 °C, 500 °C, and 650 °C. In this figure, the origin of each curve has been offset, so that the multiple curves can be distinguished. Since the serrations are significantly affected by the loading rate [71–73], all these measurements were conducted at the same target strain rate. As can be seen in Fig. 1(a), there are discrete bursts of plastic deformation that indicate localized yielding events. As expected, since the interaction of dislocations, atoms, and precipitates is different at different temperatures the serration behavior also varies [53,74].

The serration behavior in the loading section of the P-h graphs is attributed to the nucleation of the dislocations and dynamic strain aging (DSA) due to the interaction between diffusing solute atoms and mobile dislocations [54]. To pursue this further, during loading, when the nanoindenter tip is causing the deformation in the material surface, dislocations are nucleated and start their motion. However, the motion of dislocations is a discontinuous process. When dislocations encounter obstacles (like forest dislocations, precipitates, etc.) they are temporarily stopped for a short period of time. During this time, mobile interstitial elements such as carbon quickly diffuse to low energy locations, further strengthening the obstacles held on the dislocations [75,76]. Thus, dislocations' movement is further restricted by the presence of solute atoms, which leads to the temporary strengthening of the material. With an increase in the stress as a result of tip displacement, these dislocations overcome the obstacles, are released, and get away from these solute atoms and obstacles and reduce the required force for deformation [54]. However, soon they will meet another pinning point, and become re-pinned again and the process repeats [76]. Similar behavior has been seen in other solid solutions and bulk metallic glasses (BMGs) during indentation [77,78]. This was attributed to moving dislocations breaking away from the atoms in load-controlled nanoindentation and pinning/unpinning of the moving dislocations in the displacement-controlled compression experiments [5,74].

With an increase in the temperature from 300 °C to 500 °C, the ability of the solutes to diffuse to the dislocations increases [43], and pinning and unpinning phenomena that occur between the dislocations and diffusing solute atoms is enhanced [79]. Shankar et al. [18] reported that the substitutional Mo atoms are responsible for the serrated flow in Inconel 625 at temperatures lower than ~550 °C. With an increase in the temperature to 650 °C precipitates form and block the dislocation movement. This reduces the number of serrations in the P-h graph. The presence of Nb in alloy 625 leads to a hardening effect with the precipitation of the metastable γ" phase at elevated temperatures in the range of 600 °C and 750 °C (Supplementary Information, Sections 5-7, and Table S2). The precipitation of the γ" phase in crystal grain or along the grain boundaries and its interaction with mobile dislocations mitigate the DSA effect. This observation is in agreement with the one reported by Thevenet et al. [80] where they indicated that precipitation decreases the tendency for serrated flow to occur. Nalawade et al. [60] related the absence of

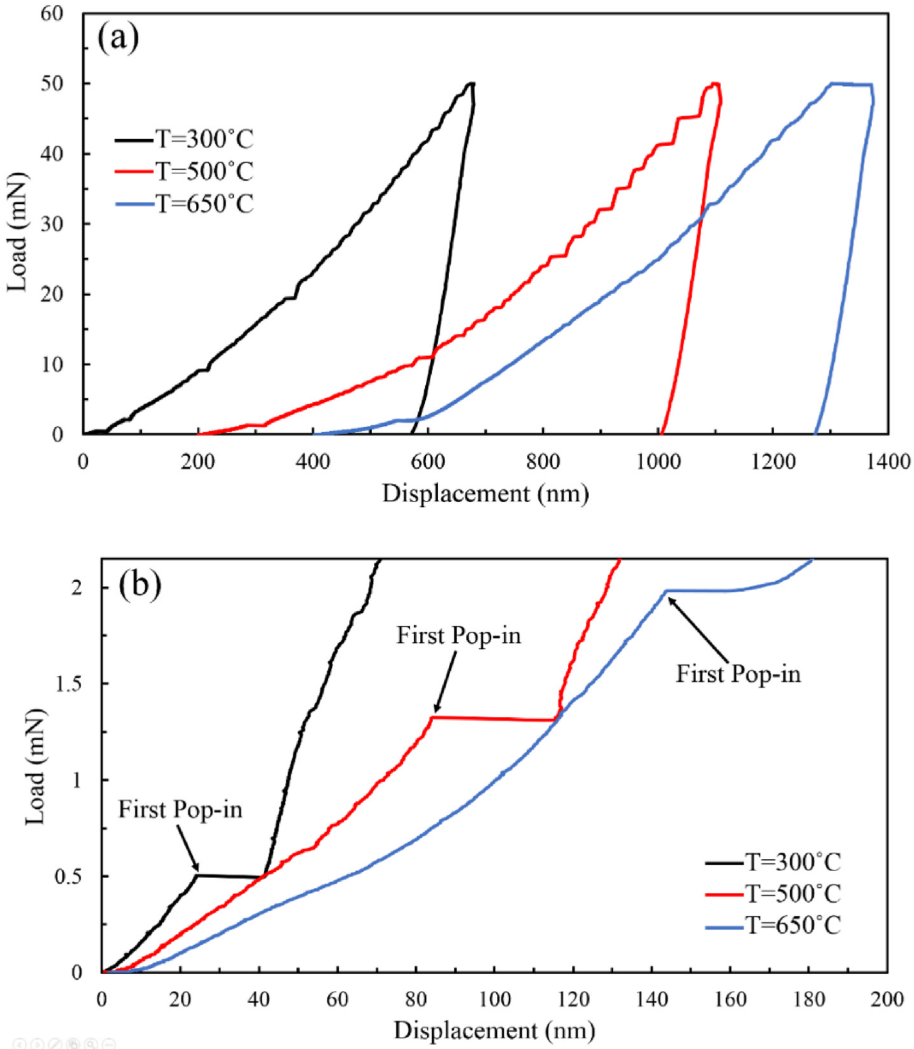

Fig. 1. (a) Load-displacement curves measured at 300 °C, 500 °C, and 650 °C, (b) a magnified view of the first pop-ins in the load-displacement graphs shown in Fig. 1(a). In Fig. 1 (a) the graphs are shifted to enhance visibility.

serrations at temperatures above ~600 °C to the depletion of niobium in the matrix as a result of the formation of precipitates. Weaver et al. [81] reported that the absence of the serrations at high temperatures is attributed to the depletion of interstitial and substitutional solutes such as Mo and Nb in the matrix due to their participation in the formation of precipitates such as Ni_3Nb (γ'') and $Ni_2(Mo)$. The presence of Mo in the specimens in this study was confirmed with the energy dispersive x-ray spectroscopy (Fig. S8, Supplementary Information), and it is predicted that a similar mechanism is happening here as well.

According to Rodriguez [51], the serrated plastic flow observed here is mostly Type D, however, a combination of Type D with other types such as Types C and E are also seen in some cases. Type D serrations are plateaus in the p-h curve and that is why Type D is also named staircase type. Type C&D are similar to type D with larger stress jumps and a sharper plateauing effect, Type E serrations do not have a pattern for the variation in the p-h curve and usually occur at higher strain. At 300 °C, the serration types were identified as Type C&D till a depth of approximately 400 nm at which point the serration type shifts to type E. For the test conducted at 500 °C the serration types appear to be a combination of types C&D and E but do not occur regularly until a depth of approximately 600 nm. For tests at 650 °C, there is a drastically reduced number of serrations, the initial pop-in serration does not have the clear plateau of a type D serration, but this is the closest one it can be characterized as and at depths greater than 800 nm they can be classified as Type E.

The presence of the serration in the force-displacement graph is an interesting result since there have been reports of the absence of DSA and serration in macroscale testing of additively manufactured IN 625 in contrast with its traditionally manufactured counterpart [6]. This is advantageous for the AM parts since DSA is undesirable in structural applications as it promotes localized deformation. Beese et al. [6] investigated the effect of microstructure, composition, and grain orientation on the presence of DSA in plastically deformed AM and TM Inconel 625. They showed that the specific microstructure of AM parts with finely dispersed secondary phases and textured grains is the reason behind this absence. Tightly spaced secondary phases such as carbides, Ni-rich phases, and Laves phase, prevent the vital carbon build-up that is required for dislocation locking and unlocking. This unique microstructure is attributed to the fabrication process in additive manufacturing with rapid heating and cooling steps. Additional tests on heat-treated AM-IN625 showed that, with partially dissolved secondary phases, DSA appeared with a low-stress drop, and with fully dissolved secondary phases, DSA appeared with a similar level stress drop as seen in TM-IN625. Beese et al. [6] stated that the serration behavior might be happening even before heat treatment of AM-IN625, but is undetectable.

As shown in Fig. 1(b), with an increase in the temperature, the first pop-in happens at a higher load. The first pop-in appears at 0.49 mN for the specimen tested at 300 °C, 1.31 mN at 500 °C, and 1.96 mN at 650 °C. Since the first pop-in is a thermally activated event under loading, a change in the pop-in load at different temperatures is expected [82]. However, the trend that is seen here is in contrast with what has been reported for other materials [83] where the first pop-in happens at progressively lower loads as the temperature is increased. This seemingly different material response is explained below based on the nucleation of dislocations as well as the formation of the strengthening phases and their interactions.

The first local perturbation and discontinuity are attributed to the dislocation activities and can be used to study the transition from purely elastic to plastic deformation, i.e., the onset of plastic flow [66]. The first major pop-in is attributed to the incipient of plastic deformation [84]. Further analysis was conducted on the first incident in 30 different measurements for each one of the temperatures (Fig. 2). As can be seen in Fig. 2, the data is distributed over a relatively wide range. The scattering of the data is due to the stochastic process of the dislocation nucleation and vacancy accumulation at the nanoscale [68,85]. Similar observations have been reported before for other materials [38,68,85].

The first pop-in events, illustrated in Fig. 2, happen at around the same load of ~1 mN for the measurements conducted at 300 °C. At higher temperatures, there is a much larger distribution range and they occur at higher values, i.e. ~1.57 mN for samples tested at 500 °C, and ~3.8 mN for samples tested at 650 °C with sporadic pop-in effects occurring up to ~11.5 mN. The statistical standard deviation for the first pop-in events was approximately 1 mN, 1.17 mN, and 3.42 mN for samples tested at 300 °C, 500 °C, and 650 °C, respectively. For nanoindentation tests using the same indenter tip and loading rate, the load at the initial pop-in event has been shown to vary [86].

Fig. 3 shows the changes in the strain rate versus displacement. The strain rate during load-controlled nanoindentation can be obtained from:

$$\dot{\varepsilon} = \frac{1}{h}\frac{dh}{dt} \tag{1}$$

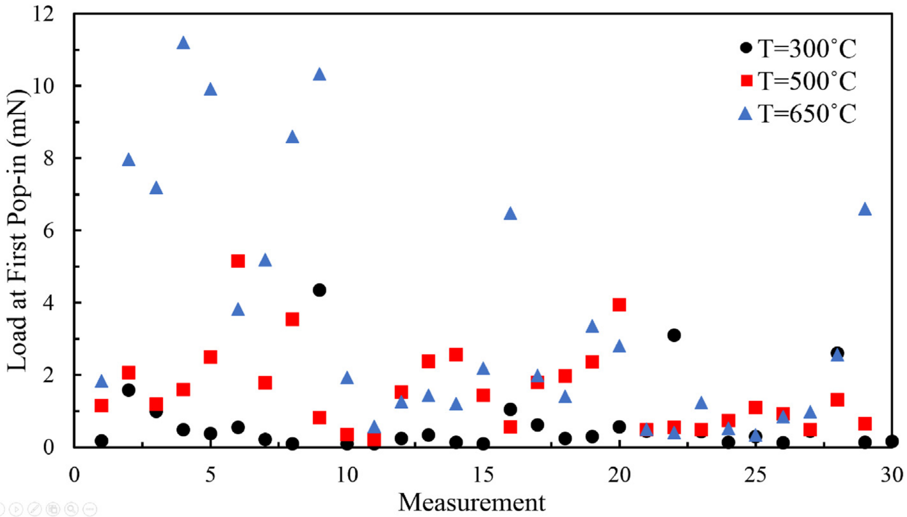

Fig. 2. The load at first pop-in events for 30 measurements at each temperature showing the statistical distributions.

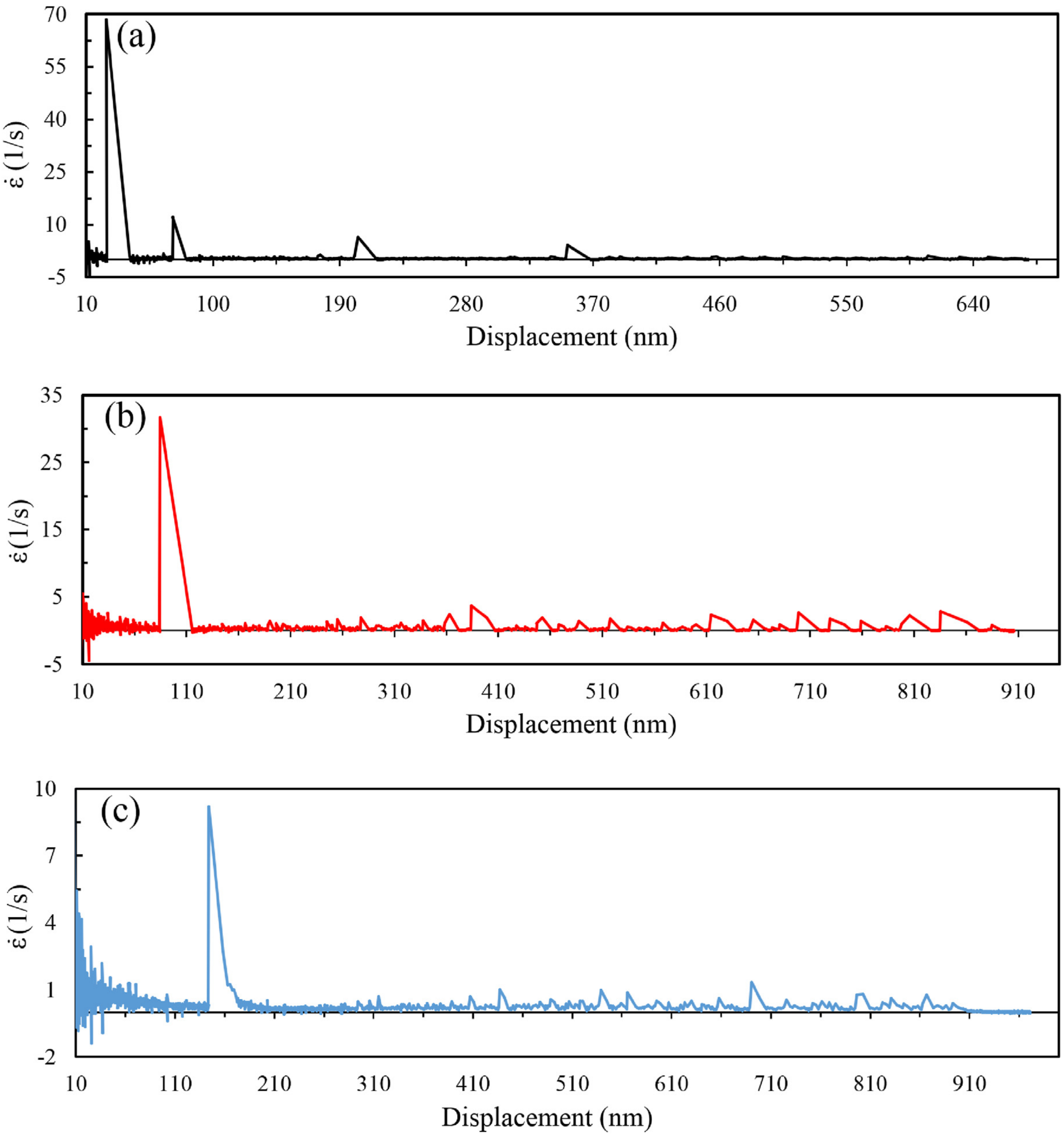

Fig. 3. Strain rate versus displacement plots for the nanoindentation experiments at (a) 300 °C, (b) 500 °C, and (c) 650 °C. The strain-rate peaks correspond to the serrations in P-h curves.

where $\dot{\varepsilon}$ is the strain rate, h is the measured depth, and t is the loading time [87]. As can be seen here, the strain rate fluctuates significantly in all three different temperatures. The peaks are more intensified at 500 °C compared with the other two tested temperatures. Interestingly, the strain rate peaks make an excellent correlation with the serrations measured in the load-displacement graphs (Fig. 1).

Fig. 4 shows displacement versus load at three different temperatures. It was reported that the depth and load relationship could be shown with a power-law relation [88]:

$$h = a + bP^{c} \tag{2}$$

where a, b, and c are fitting parameters and are dependent on the loading rate and the geometry of the indenter. As can be seen in the inset, the function with good accuracy can predict material behavior. Having this fitted curve as a baseline helps with the analysis of the underlying kinetics in the serrated flow [89–93]. By subtracting the baseline from the experimental graph, the serration events as a function of h can be calculated.

It was previously reported that the length of these pop-in provides information about the number, mobility, and interaction of dislocations that are generated underneath an indenter tip during the pop-in events [94]. Fig. 5 shows how the magnitude of the burst size (Δh) (represented by the length of the plateaus in the load-displacement curves) changes with the displacement at 300 °C, 500 °C, and 650 °C for one representative load-displacement curve at each temperature. In this figure, a burst was considered to be a plateau with a length of more than 2 nm. At each one of these temperatures, both large and small bursts are seen. Usually, large bursts are followed with smaller pop-ins (smaller Δh in Fig. 5). There

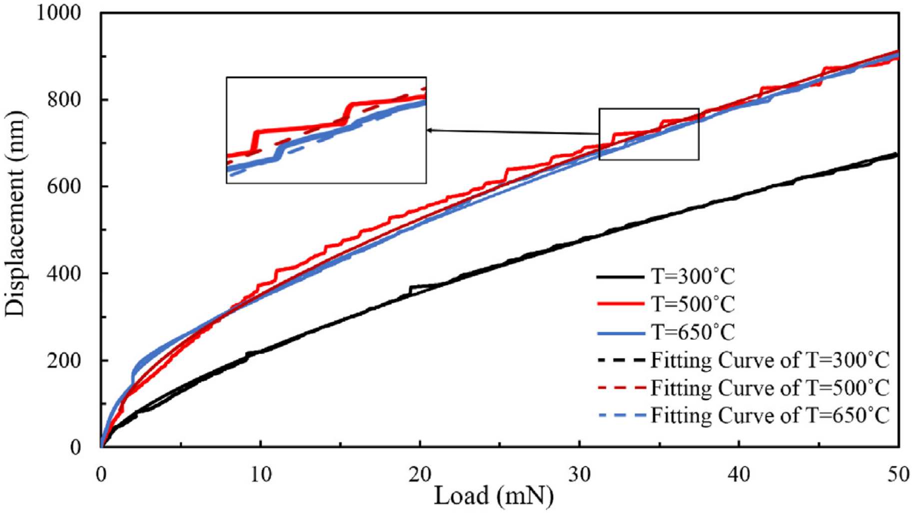

Fig. 4. Displacement-load curves at 300 °C, 500 °C, and 650 °C. The fitting curves using the power-law equation are also shown.

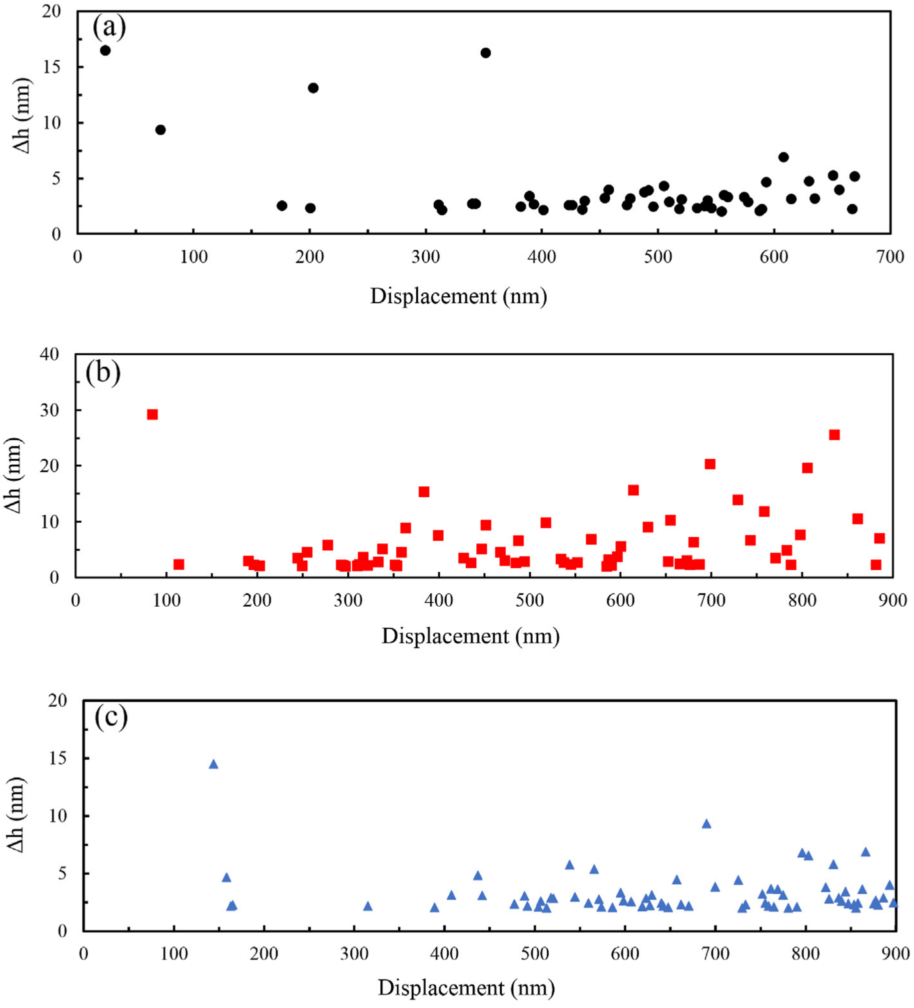

Fig. 5. Plot of Δh vs. displacement at (a) 300 °C, (b) 500 °C and (c) 650 °C.

is an increase in the elastic energy right before the first pop-in during the indentation [38]. This stored elastic energy before the first pop-in event may be partially dissipated (released) through the collective dislocation nucleation and motion during a pop-in event [95].

It can be seen that the first pop-in is the largest at the specimen tested at 500 °C, followed by the specimens tested at 300 °C and 650 °C. The mean values of serration sizes were calculated to be around 6 nm at 500 °C, larger than 4 nm, and 3.31 nm at 300 °C and

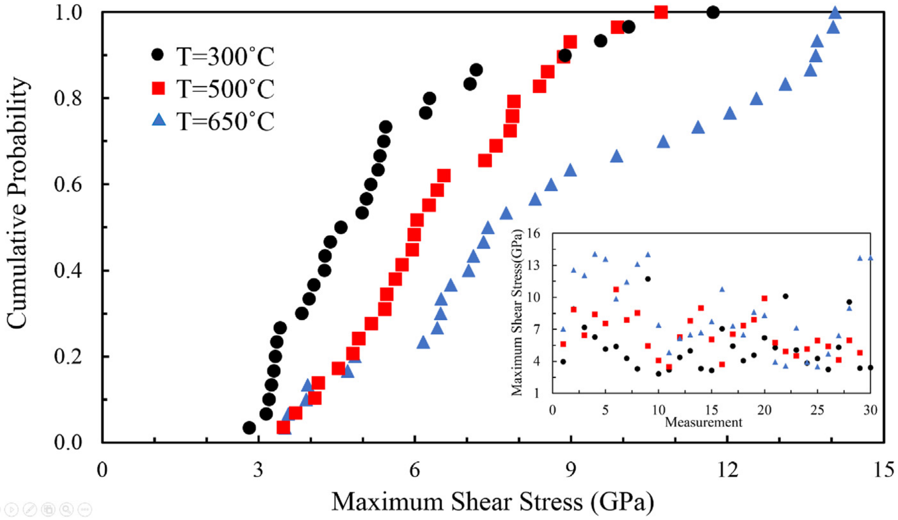

Fig. 6. Cumulative probability distributions of the maximum shear stress, τ_{max}, at the first pop-in for three different temperatures. The inset shows the distributions of maximum shear stress for 30 measurements at each temperature.

650 °C, respectively. This indicates an increase in the dislocation nucleation and mobility when the temperature has initially been increased to 500 °C. At this temperature, more significant pop-in events are promoted due to lower stresses for the nucleation and movement of the dislocations. However, at 650 °C, strengthening phases precipitate and preclude the movement of the dislocations. Similar behavior was observed in the plastic deformation region of the stress-strain curves in the tensile tests of the Inconel 625 at the temperatures of 200–700 °C [50]. While the yield point drops in macroscale tensile testing and the excursions in nanoindentation are seen at different length-scales, there are similarities in their fundamentals [96].

As can be seen in Fig. 5, there is a slight increase in the Δh values at larger strains. A possible qualitative explanation for the larger burst size at higher strains observed here is as follows. The displacement of the indenter tip is accommodated either by the activation of existing mobile dislocations or by the nucleation of dislocations in dislocation-free zones. The material shows an elastic behavior before the pop-in event, up to where a discrete volume of the material experiences shear stress that is sufficient to nucleate dislocations [38]. If the spaces between the existing dislocations are small compared to the radius of the indenter, i.e. large strains, then activation of already present dislocations happens and relatively low stresses are needed to create a plastic deformation and large Δh. When the volume where the shear stress is high beneath the indenter does not encompass pre-existing dislocation, i.e. initial loading and small strains, for plasticity to occur, the applied stress has to reach a value high enough to nucleate a dislocation [66].

Hertzian contact mechanics theory is used to estimate the components of stress and deformation in the vicinity of the contact region when the surfaces of two solid bodies come in contact. Both contacting surfaces are considered perfectly smooth, frictionless, continuous, and non-conforming. It is presumed that the deformations are in the elastic range and the strains are small [97]. Assuming Hertzian elastic contact between the indenter and the surface of the specimen at the onset of indentation, this theory can be used to predict the elastic portion of applied loads and stresses, the contact area, and the point of the first yield (first pop-in or transition from elastic to elastic-plastic deformation) [98,99]. A simple power-law relationship, $\boldsymbol{P}\propto\boldsymbol{h}^{1.5}$, consistent with the Hertzian contact solution is used to estimate the loading data before the first pop-in Ref. [97]:

$$P=\frac{4}{3}E_r\sqrt{R}h^{1.5} \tag{3}$$

Herein, P is the applied load at first pop-in, h is the measured depth, R is the radius of the indenter and E_r is the reduced indentation modulus that is related to Young's moduli, E, and Poisson's ratios, ν, of the sample and indenter through the relation:

$$\frac{1}{E_r}=\frac{1-\nu_s^2}{E_s}+\frac{1-\nu_i^2}{E_i} \tag{4}$$

Herein, The maximum shear stress that the tip induces at the moment that the dislocation nucleates during purely elastic loading can be estimated using equation [97] (5):

$$\tau_{max}=0.31\left(\frac{6E_r^2}{\pi^3R_{tip}^2}P_{pop-in}\right)^{1/3} \tag{5}$$

where E_s and υ_s are the indentation modulus and Poisson's ratio of the specimen, and E_i and υ_i are Young's modulus and Poisson's ratio of the tungsten carbide indenter, 640 GPa and 0.21 respectively [100]. The maximum shear stress for initiating the pop-in events that coincide with the onset of the plasticity of the specimens was calculated using the above equation and considering a radius of 1000 nm for the indenter tip [86,101]. The results for 30 measurements for each temperature are shown in the inset of Fig. (6). To obtain more conclusive values for the shear stress, a typical cumulative probability distribution of the maximum shear stresses for the first occurrence of pop-in at three different temperatures is plotted in Fig. 6. The maximum shear stress at 50% probability (τ_{50}) [102] was determined to be 4.6, 6.0, and 7.4 GPa for 300 °C, 500 °C, and 650 °C, respectively.

It has been previously reported that the order of the theoretical strength of crystalline metals is in the range of $\tau_{theo} = G/5 - G/30$, where G is the shear modulus of elasticity [103]. Assuming a shear modulus of elasticity of G = 81 GPa for Inconel 625 [104], it can be seen that the τ_{max} value obtained here is in the range of the τ_{theo}. These results are in perfect agreement with the previously reported data where the pop-in events occur when the τ_{max} value approaches τ_{theo} [105–107]. It is also noticeable that the maximum shear strength, τ_{max}, is increasing with the temperature. This is probably attributed to the formation of the strengthening precipitates and their complex interaction with the dislocations.

4. Conclusion

In this study, DMLS Inconel 625 samples underwent nanoindentation loading at three temperatures of 300 °C, 500 °C, and 650 °C. Load-displacement analysis was conducted at each temperature. The serrated plastic flow was characterized at all three temperatures. Though DSA and serrations were not recorded in previous AM macroscale testing, their presence in this study may be attributed to the dislocation nucleation and motion as well as their interaction with the obstacles such as other dislocations, precipitates, solute atoms. First, pop-in events were observed at all three temperatures, however, with an increase in the temperature, the first pop-in events occurred at higher loads. Strain rate peaks were found to coincide with pop-in events, which indicates the activation of dislocation motion. Pop-in events occurred when the maximum shear stress approached the theoretical shear strength. The average size of serrations were studied to explore incipient plasticity and found to increase from 4 nm at 300 °C to 6 nm at 500 °C and then decrease to 3.31 nm at 650 °C. The maximum shear strength was shown to increase with increasing the temperature. The results offer an insight into the interaction of dislocations and precipitates in additively manufactured superalloys as well as their outstanding mechanical properties at elevated temperatures. Future research using in-situ nanoindentation on AM IN625 is in progress to investigate the interaction of dislocations and precipitates as well as its impact on the serration behavior at a wider range of temperatures.

Credit authorship contribution statement

Russell A. Rowe: conducted the microstructure characterization. **Ali Tajyar:** performed the analysis of the results. **Michael Munther:** conducted the microstructure characterization. **Kurt E. Johanns:** performed the nanoindentation and helped with the analysis of the results. **Paul G. Allison:** helped with the analysis of the results. **Kasra Momeni:** helped with the analysis of the results. **Keivan Davami:** thought of the idea and designed the experiments. He wrote the manuscript with contributions of Russell Rowe and Ali Tajyar. He also performed the analysis of the results. The project was directed by Keivan Davami.

Declaration of competing interest

The authors declare that they have no known competing financial interests or personal relationships that could have appeared to influence the work reported in this paper.

Acknowledgment

This project is partly supported by DoE-ARPA-E OPEN (DE-AR0001066), and the NSF-CAREER under NSF cooperative agreement CBET-1943857. The authors would also like to thank the Alabama Transportation Institute (ATI), KLA, and ICMAS Inc. for their support of this research.

Appendix A. Supplementary data

Supplementary data to this article can be found online at https://doi.org/10.1016/j.jallcom.2020.156723.

References

[1] C. Qiu, M. al Kindi, A.S. Aladawi, I. al Hatmi, A comprehensive study on microstructure and tensile behaviour of a selectively laser melted stainless steel, Sci. Rep. 8 (2018) 1–16, https://doi.org/10.1038/s41598-018-26136-7.

[2] D. Kong, C. Dong, X. Ni, X. Li, Corrosion of metallic materials fabricated by selective laser melting, Npj Mater. Degrad. 3 (2019), https://doi.org/10.1038/s41529-019-0086-1.

[3] J.H. Martin, B.D. Yahata, J.M. Hundley, J.A. Mayer, T.A. Schaedler, T.M. Pollock, 3D printing of high-strength aluminium alloys, Nature 549 (2017) 365–369, https://doi.org/10.1038/nature23894.

[4] D. Zhang, D. Qiu, M.A. Gibson, Y. Zheng, H.L. Fraser, D.H. StJohn, M.A. Easton, Additive manufacturing of ultrafine-grained high-strength titanium alloys, Nature 576 (2019) 91–95, https://doi.org/10.1038/s41586-019-1783-1.

[5] S. Chen, W. Li, X. Xie, J. Brechtl, B. Chen, P. Li, G. Zhao, F. Yang, J. Qiao, K.A. Dahmen, P.K. Liaw, Nanoscale serration and creep characteristics of Al0.5CoCrCuFeNi high-entropy alloys, J. Alloys Compd. 752 (2018) 464–475, https://doi.org/10.1016/j.jallcom.2018.04.137.

[6] A.M. Beese, Z. Wang, A.D. Stoica, D. Ma, Absence of dynamic strain aging in an additively manufactured nickel-base superalloy, Nat. Commun. 9 (2018) 1–8, https://doi.org/10.1038/s41467-018-04473-5.

[7] E. Hosseini, V.A. Popovich, A review of mechanical properties of additively manufactured Inconel 718, Addit. Manuf. 30 (2019), 100877, https://doi.org/10.1016/j.addma.2019.100877.

[8] T.G. Gallmeyer, S. Moorthy, B.B. Kappes, M.J. Mills, B. Amin-Ahmadi, A.P. Stebner, Knowledge of process-structure-property relationships to engineer better heat treatments for laser powder bed fusion additive manufactured Inconel 718, Addit. Manuf. 31 (2020), 100977, https://doi.org/10.1016/j.addma.2019.100977.

[9] L. Yan, Y. Chen, F. Liou, Additive manufacturing of functionally graded metallic materials using laser metal deposition, Addit. Manuf. 31 (2020), 100901, https://doi.org/10.1016/j.addma.2019.100901.

[10] Q. Han, Y. Gu, R. Setchi, F. Lacan, R. Johnston, S.L. Evans, S. Yang, Additive manufacturing of high-strength crack-free Ni-based Hastelloy X superalloy, Addit. Manuf. 30 (2019), 100919, https://doi.org/10.1016/j.addma.2019.100919.

[11] H. Springer, C. Baron, F. Mostaghimi, J. Poveleit, L. Mädler, V. Uhlenwinkel, Additive manufacturing of high modulus steels: new possibilities for lightweight design, Addit. Manuf. 32 (2020), 101033, https://doi.org/10.1016/j.addma.2019.101033.

[12] J. Kranz, D. Herzog, C. Emmelmann, Design guidelines for laser additive manufacturing of lightweight structures in TiAl6V4, J. Laser Appl. 27 (2015) S14001, https://doi.org/10.2351/1.4885235.

[13] M. Donachie, S. Donachie, Superalloys: A Technical Guide, second ed., ASM International, 2002. https://www.asminternational.org/search/-/journal_content/56/10192/06128G/PUBLICATION. (Accessed 20 April 2020).

[14] J. Nguejio, F. Szmytka, S. Hallais, A. Tanguy, S. Nardone, M. Godino Martinez, Comparison of microstructure features and mechanical properties for additive manufactured and wrought nickel alloys 625, Mater. Sci. Eng. 764 (2019), 138214, https://doi.org/10.1016/j.msea.2019.138214.

[15] C. Li, R. White, X.Y. Fang, M. Weaver, Y.B. Guo, Microstructure evolution characteristics of Inconel 625 alloy from selective laser melting to heat treatment, Mater. Sci. Eng. 705 (2017) 20–31, https://doi.org/10.1016/j.msea.2017.08.058.

[16] S. Li, Q. Wei, Y. Shi, C.K. Chua, Z. Zhu, D. Zhang, Microstructure characteristics of inconel 625 superalloy manufactured by selective laser melting, J. Mater. Sci. Technol. 31 (2015) 946–952, https://doi.org/10.1016/j.jmst.2014.09.020.

[17] L.M. Suave, J. Cormier, P. Villechaise, A. Soula, Z. Hervier, D. Bertheau, J. Laigo, Microstructural evolutions during thermal aging of alloy 625: impact of temperature and forming process, Metall. Mater. Trans.: Phys. Metal. Mater. Sci. 45 (2014) 2963–2982, https://doi.org/10.1007/s11661-014-2256-7.

[18] V. Shankar, M. Valsan, K.B.S. Rao, S.L. Mannan, Effects of temperature and strain rate on tensile properties and activation energy for dynamic strain aging in alloy 625, Metall. Mater. Trans.: Phys. Metal. Mater. Sci. 35 (2004) 3129–3139, https://doi.org/10.1007/s11661-004-0057-0.

[19] L.M. Suave, D. Bertheau, J. Cormier, P. Villechaise, A. Soula, Z. Hervier, J. Laigo, Impact of microstructural evolutions during thermal aging of Alloy 625 on its monotonic mechanical properties, MATEC Web Conf. 14 (2014), https://doi.org/10.1051/matecconf/20141421001.

[20] V. Shankar, K. Bhanu Sankara Rao, S.L. Mannan, Microstructure and mechanical properties of Inconel 625 superalloy, J. Nucl. Mater. 288 (2001) 222–232, https://doi.org/10.1016/S0022-3115(00)00723-6.

[21] K. Davami, M. Mohsenizadeh, M. Mitcham, P. Damasus, Q. Williams, M. Munther, Additively manufactured self-healing structures with embedded healing agent reservoirs, Sci. Rep. 9 (2019) 1–8, https://doi.org/10.1038/s41598-019-43883-3.

[22] K. Kese, P.A.T. Olsson, A.M. Alvarez Holston, E. Broitman, High temperature nanoindentation hardness and Young's modulus measurement in a neutron-irradiated fuel cladding material, J. Nucl. Mater. 487 (2017) 113–120, https://doi.org/10.1016/j.jnucmat.2017.02.014.

[23] M. Munther, T. Palma, F. Tavangarian, A. Beheshti, K. Davami, Nanomechanical properties of additively and traditionally manufactured nickel-chromium-based superalloys through instrumented nanoindentation, Manuf. Lett. 23 (2020) 39–43, https://doi.org/10.1016/j.mfglet.2019.09.003.

[24] M. Sadeghilaridjani, S. Mukherjee, High-temperature nano-indentation

creep behavior of multi-principal element alloys under static and dynamic loads, Metals 10 (2020), https://doi.org/10.3390/met10020250.
[25] T. Palma, M. Munther, P. Damasus, S. Salari, A. Beheshti, K. Davami, Multiscale mechanical and tribological characterizations of additively manufactured polyamide 12 parts with different print orientations, J. Manuf. Process. 40 (2019) 76–83, https://doi.org/10.1016/j.jmapro.2019.03.004.
[26] B. Paul, A. Sarkar, J. Kishor, S. Majumdar, Studies on creep and wear behavior of Mo-40Ti-10Si alloy prepared by hot pressing, J. Mater. Eng. Perform. 29 (2020) 1007–1014, https://doi.org/10.1007/s11665-020-04603-5.
[27] H. Attar, S. Ehtemam-Haghighi, D. Kent, I.v. Okulov, H. Wendrock, M. Bönisch, A.S. Volegov, M. Calin, J. Eckert, M.S. Dargusch, Nanoindentation and wear properties of Ti and Ti-TiB composite materials produced by selective laser melting, Mater. Sci. Eng. 688 (2017) 20–26, https://doi.org/10.1016/j.msea.2017.01.096.
[28] Y. Hong, C. Zhou, Y. Zheng, L. Zhang, J. Zheng, X. Chen, Effect of hydrogen and strain rate on nanoindentation creep of austenitic stainless steel, Int. J. Hydrogen Energy 44 (2019) 1253–1262, https://doi.org/10.1016/j.ijhydene.2018.11.017.
[29] D. Bufford, Y. Liu, J. Wang, H. Wang, X. Zhang, In situ nanoindentation study on plasticity and work hardening in aluminium with incoherent twin boundaries, Nat. Commun. 5 (2014), https://doi.org/10.1038/ncomms5864.
[30] M. Rozmus-Górnikowska, J. Kusiński, Ł. Cieniek, Effect of laser shock peening on the microstructure and properties of the inconel 625 surface layer, J. Mater. Eng. Perform. 29 (2020) 1544–1549, https://doi.org/10.1007/s11665-020-04667-3.
[31] H. Wang, A. Dhiman, H.E. Ostergaard, Y. Zhang, T. Siegmund, J.J. Kruzic, V. Tomar, Nanoindentation based properties of Inconel 718 at elevated temperatures: a comparison of conventional versus additively manufactured samples, Int. J. Plast. 120 (2019) 380–394, https://doi.org/10.1016/j.ijplas.2019.04.018.
[32] C.F.O. Dahlberg, Y. Saito, M.S. Öztop, J.W. Kysar, Geometrically necessary dislocation density measurements associated with different angles of indentations, Int. J. Plast. 54 (2014) 81–95, https://doi.org/10.1016/j.ijplas.2013.08.008.
[33] E. Renner, Y. Gaillard, F. Richard, F. Amiot, P. Delobelle, Sensitivity of the residual topography to single crystal plasticity parameters in Berkovich nanoindentation on FCC nickel, Int. J. Plast. 77 (2016) 118–140, https://doi.org/10.1016/j.ijplas.2015.10.002.
[34] S. Xu, R. Che, L. Xiong, Y. Chen, D.L. McDowell, A quasistatic implementation of the concurrent atomistic-continuum method for FCC crystals, Int. J. Plast. 72 (2015) 91–126, https://doi.org/10.1016/j.ijplas.2015.05.007.
[35] P.A. Sabnis, S. Forest, N.K. Arakere, V.A. Yastrebov, Crystal plasticity analysis of cylindrical indentation on a Ni-base single crystal superalloy, Int. J. Plast. 51 (2013) 200–217, https://doi.org/10.1016/j.ijplas.2013.05.004.
[36] C. Qiu, H. Chen, Q. Liu, S. Yue, H. Wang, On the solidification behaviour and cracking origin of a nickel-based superalloy during selective laser melting, Mater. Char. 148 (2019) 330–344, https://doi.org/10.1016/j.matchar.2018.12.032.
[37] T. Palma, M. Munther, M. Sharma, L. Hackel, A. Beheshti, K. Davami, Nanomechanical characterization of laser peened additively manufactured inconel 718 superalloy, Adv. Eng. Mater. 21 (2019), 1900499, https://doi.org/10.1002/adem.201900499.
[38] G. Stenerud, R. Johnsen, J.S. Olsen, J. He, A. Barnoush, Effect of hydrogen on dislocation nucleation in alloy 718, Int. J. Hydrogen Energy 42 (2017) 15933–15942, https://doi.org/10.1016/j.ijhydene.2017.04.290.
[39] M. Abbadi, P. Hähner, A. Zeghloul, On the characteristics of Portevin - le Chatelier bands in aluminum alloy 5182 under stress-controlled and strain-controlled tensile testing, Mater. Sci. Eng. 337 (2002) 194–201, https://doi.org/10.1016/S0921-5093(02)00036-9.
[40] A. van den Beukel, U.F. Kocks, The strain dependence of static and dynamic strain-aging, Acta Metall. 30 (1982) 1027–1034, https://doi.org/10.1016/0001-6160(82)90211-5.
[41] S.D. Antolovich, R.W. Armstrong, Plastic strain localization in metals: origins and consequences, Prog. Mater. Sci. 59 (2014) 1–160, https://doi.org/10.1016/j.pmatsci.2013.06.001.
[42] Y. Brechet, Y. Estrin, On the influence of precipitation on the Portevin-Le Chatelier effect, Acta Metall. Mater. 43 (1995) 955–963, https://doi.org/10.1016/0956-7151(94)00334-E.
[43] G. Ananthakrishna, Current theoretical approaches to collective behavior of dislocations, Phys. Rep. 440 (2007) 113–259, https://doi.org/10.1016/j.physrep.2006.10.003.
[44] S.L. Mannan, Role of dynamic strain ageing in low cycle fatigue, Bull. Mater. Sci. 16 (1993) 561–582, https://doi.org/10.1007/BF02757656.
[45] A. van den Beukel, Theory of the effect of dynamic strain aging on mechanical properties, Phys. Status Solidi 30 (1975) 197–206, https://doi.org/10.1002/pssa.2210300120.
[46] A. den Beukel, On the mechanism of serrated yielding and dynamic strain ageing, Acta Metall. 28 (1980) 965–969.
[47] E. Rizzi, P. Hähner, On the Portevin-Le Chatelier effect: theoretical modeling and numerical results, Int. J. Plast. 20 (2004) 121–165, https://doi.org/10.1016/S0749-6419(03)00035-4.
[48] D.J. Lloyd, D.W. Chung, M.C. Chaturvedi, Serrated Yielding in a Super Alloy 40Co-38Ni-17Cr-5Ti, 1975, p. 23.
[49] K.B.S. Rao, S. Kalluri, G.R. Halford, M.A. McGaw, Serrated flow and deformation substructure at room temperature in Inconel 718 superalloy during strain controlled fatigue, Scripta Metall. Mater. 32 (1995) 493–498, https://doi.org/10.1016/0956-716X(95)90826-6.
[50] M.M. de Oliveira, A.A. Couto, G.F.C. Almeida, D.A.P. Reis, N.B. de Lima, R. Baldan, Mechanical behavior of inconel 625 at elevated temperatures, Metals 9 (2019), https://doi.org/10.3390/met9030301.
[51] P. Rodriguez, Serrated plastic flow, Bull. Mater. Sci. 6 (1984) 653–663, https://doi.org/10.1007/BF02743993.
[52] A. Rauf, C.Y. Guo, Y.N. Fang, Z. Yu, B.A. Sun, T. Feng, Binary Cu-Zr thin film metallic glasses with tunable nanoscale structures and properties, J. Non-Cryst. Solids 498 (2018) 95–102, https://doi.org/10.1016/j.jnoncrysol.2018.06.015.
[53] S. Chen, X. Xie, W. Li, R. Feng, B. Chen, J. Qiao, Y. Ren, Y. Zhang, K.A. Dahmen, P.K. Liaw, Temperature effects on the serrated behavior of an Al0.5CoCrCuFeNi high-entropy alloy, Mater. Chem. Phys. 210 (2018) 20–28, https://doi.org/10.1016/j.matchemphys.2017.09.004.
[54] W. Ziaja, M. Poręba, M. Motyka, Plasticity of nickel-based superalloy 625 at elevated temperature, Adv. Manuf. Sci. Technol. 41 (2017) 41–49, https://doi.org/10.2478/amst-2017-0021.
[55] A. Yilmaz, The Portevin-Le Chatelier effect: a review of experimental findings, Sci. Technol. Adv. Mater. 12 (2011), https://doi.org/10.1088/1468-6996/12/6/063001.
[56] M. Weisse, C.K. Wamukwamba, H.J. Christ, H. Mughrabi, The cyclic deformation and fatigue behaviour of the low carbon steel SAE 1045 in the temperature regime of dynamic strain ageing, Acta Metall. Mater. 41 (1993) 2227–2233, https://doi.org/10.1016/0956-7151(93)90392-6.
[57] D. Delafosse, G. Lapasset, L.P. Kubin, Dynamic strain ageing and crack propagation in the 2091 Al-Li alloy, Scripta Metall. Mater. 29 (1993) 1379–1384, https://doi.org/10.1016/0956-716X(93)90323-K.
[58] M. Valsan, D.H. Sastry, K.B. sankara Rao, S.L. Mannan, Effect of strain rate on the high-temperature low-cycle fatigue properties of a nimonic PE-16 superalloy, Metall. Mater. Trans. 25 (1994) 159–171, https://doi.org/10.1007/BF02646684.
[59] M. Hörnqvist, C. Joseph, C. Persson, J. Weidow, H. Lai, Dynamic Strain Aging in Haynes 282 Superalloy, MATEC Web of Conferences, vol.14, 2014, https://doi.org/10.1051/matecconf/20141416002, 0–5.
[60] S.A. Nalawade, M. Sundararaman, R. Kishore, J.G. Shah, The influence of aging on the serrated yielding phenomena in a nickel-base superalloy, Scripta Mater. 59 (2008) 991–994, https://doi.org/10.1016/j.scriptamat.2008.07.004.
[61] Y.C. Lin, H. Yang, Y. Xin, C.Z. Li, Effects of initial microstructures on serrated flow features and fracture mechanisms of a nickel-based superalloy, Mater. Char. 144 (2018) 9–21, https://doi.org/10.1016/j.matchar.2018.06.029.
[62] P. Maj, J. Zdunek, J. Mizera, K.J. Kurzydlowski, B. Sakowicz, M. Kaminski, Microstructure and strain-stress analysis of the dynamic strain aging in inconel 625 at high temperature, Met. Mater. Int. 23 (2017) 54–67, https://doi.org/10.1007/s12540-017-6264-1.
[63] Z. Wang, H. Bei, E.P. George, G.M. Pharr, Influences of surface preparation on nanoindentation pop-in in single-crystal Mo, Scripta Mater. 65 (2011) 469–472, https://doi.org/10.1016/j.scriptamat.2011.05.030.
[64] C.A. Schuh, J.K. Mason, A.C. Lund, A.M. Hodge, High temperature nanoindentation for the study of flow defects, in: Materials Research Society Symposium Proceedings, 2005, pp. 153–158, https://doi.org/10.1557/proc-841-r4.8.
[65] N.I. Tymiak, D.E. Kramer, D.F. Bahr, T.J. Wyrobek, W.W. Gerberich, Plastic strain and strain gradients at very small indentation depths, Acta Mater. 49 (2001) 1021–1034, https://doi.org/10.1016/S1359-6454(00)00378-5.
[66] S. Shim, H. Bei, E.P. George, G.M. Pharr, A different type of indentation size effect, Scripta Mater. 59 (2008) 1095–1098, https://doi.org/10.1016/j.scriptamat.2008.07.026.
[67] H. Somekawa, C.A. Schuh, Effect of solid solution elements on nanoindentation hardness, rate dependence, and incipient plasticity in fine grained magnesium alloys, Acta Mater. 59 (2011) 7554–7563, https://doi.org/10.1016/j.actamat.2011.08.047.
[68] Y. Ma, X. Huang, W. Hang, M. Liu, J. Yuan, T. Zhang, On the delayed incipient plastic deformation in a LiTaO3 single crystal by nanoindentation, J. Phys. Appl. Phys. (2020), https://doi.org/10.1088/1361-6463/ab6f8c.
[69] V. Maier-Kiener, K. Durst, Advanced nanoindentation testing for studying strain-rate sensitivity and activation volume, JOM (J. Occup. Med.) 69 (2017) 2246–2255, https://doi.org/10.1007/s11837-017-2536-y.
[70] W.C. Oliver, G.M. Pharr, An improved technique for determining hardness and elastic modulus using load and displacement sensing indentation experiments, J. Mater. Res. 7 (1992) 1564–1583, https://doi.org/10.1557/JMR.1992.1564.
[71] C.A. Schuh, A.C. Lund, T.G. Nieh, New regime of homogeneous flow in the deformation map of metallic glasses: elevated temperature nanoindentation experiments and mechanistic modeling, Acta Mater. 52 (2004) 5879–5891, https://doi.org/10.1016/j.actamat.2004.09.005.
[72] G. Liao, Z. Long, M. Zhao, M. Zhong, W. Liu, W. Chai, Serrated flow behavior in a Pd-based bulk metallic glass under nanoindentation, J. Non-Cryst. Solids 460 (2017) 47–53, https://doi.org/10.1016/j.jnoncrysol.2017.01.010.
[73] C.A. Schuh, A.S. Argon, T.G. Nieh, J. Wadsworth, The transition from localized to homogeneous plasticity during nanoindentation of an amorphous metal, Phil. Mag. 83 (2003) 2585–2597, https://doi.org/10.1080/1478643031000118012.
[74] S. Chen, X. Xie, B. Chen, J. Qiao, Y. Zhang, Y. Ren, K.A. Dahmen, P.K. Liaw, Effects of temperature on serrated flows of Al0.5CoCrCuFeNi high-entropy alloy, JOM (J. Occup. Med.) 67 (2015) 2314–2320, https://doi.org/10.1007/s11837-015-1580-8.
[75] C.L. Hale, W.S. Rollings, M.L. Weaver, Activation energy calculations for discontinuous yielding in inconel 718SPF, Mater. Sci. Eng. 300 (2001)

153–164, https://doi.org/10.1016/S0921-5093(00)01470-2.

[76] A. Sawant, S. Tin, J.C. Zhao, High temperature nanoindentation of ni-base superalloys, Proc. Int. Symp. Superalloys (2008) 863–871, https://doi.org/10.7449/2008/superalloys_2008_863_871.

[77] B.C. Wei, T.H. Zhang, W.H. Li, Y.F. Sun, Y. Yu, Y.R. Wang, Serrated plastic flow during nanoindentation in Nd-based bulk metallic glasses, in: Intermetallics, Elsevier, 2004, pp. 1239–1243, https://doi.org/10.1016/j.intermet.2004.04.030.

[78] N.Q. Chinh, G. Horváth, Z. Kovács, J. Lendvai, Characterization of plastic instability steps occurring in depth-sensing indentation tests, Mater. Sci. Eng. 324 (2002) 219–224, https://doi.org/10.1016/S0921-5093(01)01315-6.

[79] Y. Cai, C. Tian, S. Fu, G. Han, C. Cui, Q. Zhang, Influence of γ' precipitates on Portevin-Le Chatelier effect of NI-based superalloys, Mater. Sci. Eng. 638 (2015) 314–321, https://doi.org/10.1016/j.msea.2015.04.033.

[80] D. Thevenet, M. Mliha-Touati, A. Zeghloul, The effect of precipitation on the Portevin-Le Chatelier effect in an Al-Zn-Mg-Cu alloy, Mater. Sci. Eng. 266 (1999) 175–182, https://doi.org/10.1016/S0921-5093(99)00029-5.

[81] M.L. Weaver, C.S. Hale, Effects of precipitation on serrated yielding in inconel 718, Proc. Int. Symp. Superalloys Various Derivatives 1 (2001) 421–432, https://doi.org/10.7449/2001/superalloys_2001_421_432.

[82] Y. Sato, S. Shinzato, T. Ohmura, S. Ogata, Atomistic prediction of the temperature- and loading-rate-dependent first pop-in load in nanoindentation, Int. J. Plast. 121 (2019) 280–292, https://doi.org/10.1016/j.ijplas.2019.06.012.

[83] A.C. Lund, A.M. Hodge, C.A. Schuh, Incipient plasticity during nanoindentation at elevated temperatures, Appl. Phys. Lett. 85 (2004) 1362–1364, https://doi.org/10.1063/1.1784891.

[84] A.M. Minor, J.W. Morris, E.A. Stach, Quantitative in situ nanoindentation in an electron microscope, Appl. Phys. Lett. 79 (2001) 1625–1627, https://doi.org/10.1063/1.1400768.

[85] X. Lu, Y. Ma, M. Zamanzade, Y. Deng, D. Wang, W. Bleck, W.W. Song, A. Barnoush, Insight into hydrogen effect on a duplex medium-Mn steel revealed by in-situ nanoindentation test, Int. J. Hydrogen Energy 44 (2019) 20545–20551, https://doi.org/10.1016/j.ijhydene.2019.04.290.

[86] C.A. Schuh, A.C. Lund, Application of nucleation theory to the rate dependence of incipient plasticity during nanoindentation, J. Mater. Res. 19 (2004) 2152–2158, https://doi.org/10.1557/JMR.2004.0276.

[87] R. Goodall, T.W. Clyne, A critical appraisal of the extraction of creep parameters from nanoindentation data obtained at room temperature, Acta Mater. 54 (2006) 5489–5499, https://doi.org/10.1016/j.actamat.2006.07.020.

[88] I.N. Sneddon, The relation between load and penetration in the axisymmetric boussinesq problem for a punch of arbitrary profile, Int. J. Eng. Sci. 3 (1965) 47–57, https://doi.org/10.1016/0020-7225(65)90019-4.

[89] J.W. Qiao, Y. Zhang, P.K. Liaw, Serrated flow kinetics in a Zr-based bulk metallic glass, Intermetallics 18 (2010) 2057–2064, https://doi.org/10.1016/j.intermet.2010.06.013.

[90] X.L. Bian, G. Wang, K.C. Chan, J.L. Ren, Y.L. Gao, Q.J. Zhai, Shear avalanches in metallic glasses under nanoindentation: deformation units and rate dependent strain burst cut-off, Appl. Phys. Lett. 103 (2013), 101907, https://doi.org/10.1063/1.4820782.

[91] W. Peng, B. Wei, T. Zhang, Y. Liu, L. Li, Characterization of shear banding in La-based bulk metallic glasses through indentation, Mater. Trans. 48 (2007) 1759–1764, https://doi.org/10.2320/matertrans.MJ200761.

[92] M. Zhang, Y.J. Wang, L.H. Dai, Understanding the serrated flow and Johari-Goldstein relaxation of metallic glasses, J. Non-Cryst. Solids 444 (2016) 23–30, https://doi.org/10.1016/j.jnoncrysol.2016.04.036.

[93] H. Li, A.H.W. Ngan, M.G. Wang, Continuous strain bursts in crystalline and amorphous metals during plastic deformation by nanoindentation, J. Mater. Res. 20 (2005) 3072–3081, https://doi.org/10.1557/JMR.2005.0379.

[94] C.A. Schuh, Nanoindentation studies of materials, Mater. Today 9 (2006) 32–40, https://doi.org/10.1016/S1369-7021(06)71495-X.

[95] W.G. Mao, Y.G. Shen, C. Lu, Deformation behavior and mechanical properties of polycrystalline and single crystal alumina during nanoindentation, Scripta Mater. 65 (2011) 127–130, https://doi.org/10.1016/j.scriptamat.2011.03.022.

[96] T.H. Ahn, C.S. Oh, K. Lee, E.P. George, H.N. Han, Relationship between yield point phenomena and the nanoindentation pop-in behavior of steel, J. Mater. Res. 27 (2012) 39–44, https://doi.org/10.1557/jmr.2011.208.

[97] K.L. Johnson, K.L. Johnson, Contact Mechanics, Cambridge University Press, 1987. https://books.google.com/books?id=Do6WQlUwbpkC.

[98] P. Sudharshan Phani, K.E. Johanns, E.P. George, G.M. Pharr, A stochastic model for the size dependence of spherical indentation pop-in, J. Mater. Res. 28 (2013) 2728–2739, https://doi.org/10.1557/jmr.2013.254.

[99] A.K. Nanda Kumar, M.D. Kannan, S. Jayakumar, K.S. Rajam, V.S. Raju, Investigations on the mechanical behaviour of rough surfaces of TiNi thin films by nano indentation studies, Surf. Coating. Technol. 201 (2006) 3253–3259, https://doi.org/10.1016/j.surfcoat.2006.06.053.

[100] M. Koopman, Z.Z. Fang, X. Wang, P.K. Mehrotra, Properties and selection of cemented carbides, Powder Metall. 7 (2015), https://doi.org/10.31399/asm.hb.v07.a0006064, 0.

[101] I.C. Choi, Y. Zhao, Y.J. Kim, B.G. Yoo, J.Y. Suh, U. Ramamurty, J. il Jang, Indentation size effect and shear transformation zone size in a bulk metallic glass in two different structural states, Acta Mater. 60 (2012) 6862–6868, https://doi.org/10.1016/j.actamat.2012.08.061.

[102] X.K. Zhang, J.C. Huang, P.H. Lin, W.S. Chuang, T.Y. Liu, Y.C. Wu, Y.C. Liao, J.S.C. Jang, Effect of orientation and loading rate on the incipient behavior of Ti60(AlCrVNb)40 medium entropy alloy, Mater. Sci. Eng. 775 (2020), https://doi.org/10.1016/j.msea.2020.138969.

[103] Robert W.K. Honeycombe, The Plastic Deformation of Metals, Edward Arnold, 1968.

[104] Y. Gao, M. Zhou, Superior mechanical behavior and fretting wear resistance of 3D-printed Inconel 625 superalloy, Appl. Sci. 8 (2018), https://doi.org/10.3390/app8122439.

[105] W.W. Gerberich, J.C. Nelson, E.T. Lilleodden, P. Anderson, J.T. Wyrobek, Indentation induced dislocation nucleation: the initial yield point, Acta Mater. 44 (1996) 3585–3598, https://doi.org/10.1016/1359-6454(96)00010-9.

[106] A. Gouldstone, H.J. Koh, K.Y. Zeng, A.E. Giannakopoulos, S. Suresh, Discrete and continuous deformation during nanoindentation of thin films, Acta Mater. 48 (2000) 2277–2295, https://doi.org/10.1016/S1359-6454(00)00009-4.

[107] H. Bei, Y.F. Gao, S. Shim, E.P. George, G.M. Pharr, Strength differences arising from homogeneous versus heterogeneous dislocation nucleation, Phys. Rev. B Condens. Matter 77 (2008), 060103, https://doi.org/10.1103/PhysRevB.77.060103.